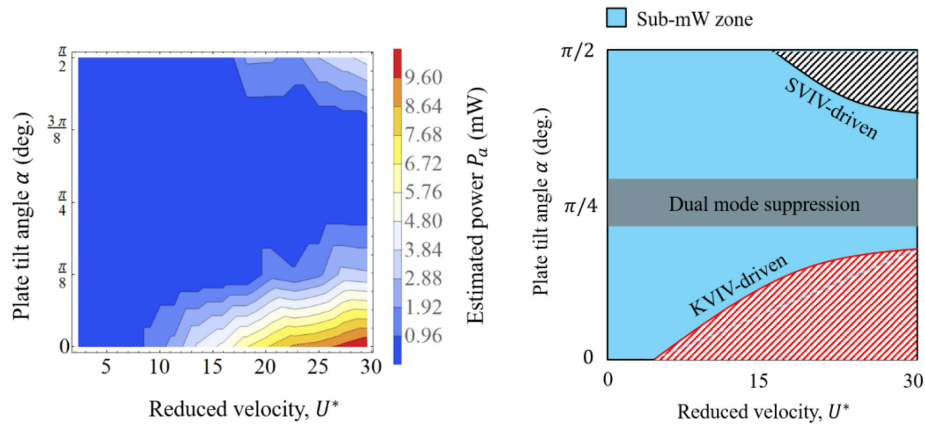


Graphical Abstract

Vortex-induced Vibration of an Angled Cruciform for Energy Harvesting

Ahmad Adzlan, Mohamed Sukri Mat Ali, Sheikh Ahmad Zaki



Highlights

Vortex-induced Vibration of an Angled Cruciform for Energy Harvesting

Ahmad Adzlan,Mohamed Sukri Mat Ali,Sheikh Ahmad Zaki

- Three main energy harvesting regimes were identified, based on the cruciform angle
- The streamwise-vortex induced vibration regime produces power in the order of 1 mW
- Power output is below 1 mW between angles 67.5° and 22.5°
- Power output can achieve up to 10 mW, as the angle is brought closer to 0° .

Vortex-induced Vibration of an Angled Cruciform for Energy Harvesting

Ahmad Adzlan^{a,b,*}, Mohamed Sukri Mat Ali^a and Sheikh Ahmad Zaki^a

^aMalaysia-Japan International Institute of Technology, Universiti Teknologi Malaysia, 54200 Kuala Lumpur, Malaysia

^bFaculty of Engineering, Universiti Malaysia Sarawak, 94300 Kota Samarahan, Sarawak, Malaysia

ARTICLE INFO

Keywords:

Vortex-induced vibration
Vibration energy harvester
CFD simulation
Streamwise vorticity
Ensemble empirical mode decomposition (EEMD)
Hilbert transform

ABSTRACT

We investigated the displacement and lift time series of a circular cylinder - strip plate cruciform system for energy harvesting in the Reynolds number range $1.1 \times 10^3 \leq Re \leq 14.6 \times 10^3$, numerically using the open source C++ library: OpenFOAM. The Karman vortex-induced vibration (KVIV) regime was identified between reduced velocity, U^* , 2.3 and 13.6, while the streamwise vortex-induced vibration (SVIV) regime was identified between $18.2 \leq U^* \leq 29.5$. We analysed the cylinder displacement and lift time series using the Hilbert-Huang transform (HHT). Within this range of U^* , Karman vortex shedding contributes nearly as much as streamwise vortex shedding to the root-mean-square amplitude of total lift, while between $25.0 \leq U^* \leq 29.5$, the Karman component contribution is on average twice that of the streamwise component. These findings hint at the possibility to improve the power output of the harvester by a factor of two between $18.2 \leq U^* \leq 22.7$ and by a factor of three between $25.0 \leq U^* \leq 29.5$, if we can unite the contribution to the root-mean-square amplitude of the total lift under a single vibration-driving mechanism: the shedding of streamwise vortex.

1. Introduction

Streamwise vortex-induced vibration (SVIV) is a type of vortex-induced vibration (VIV) driven by vortical structures whose vorticity vector points in the direction of the free stream. In recent decades, there have been efforts to exploit the SVIV phenomenon from cruciform structures for energy harvesting, an example of which is given in Fig. The literature on this subject can be broadly categorised into two groups: how the mechanical properties of the oscillator (e.g., mass ratio, damping, etc.) affects the amplitude/frequency response of SVIV (Koide et al., 2009, 2013; Nguyen et al., 2012) and how the minutiae of the flow field affect the force driving the vibration of the cylinder, i.e. the fluid mechanical aspect of the system (Deng et al., 2007; Koide et al., 2017; Zhao and Lu, 2018).

In the first focus area, researchers studied some permutation of the following method to convert the vibration into electrical power. The method consists of a coil and magnet. The coil, which moves with the vibrating cylinder, creates relative motion against the magnet, which is placed in the hollow of the coil (Koide et al., 2009). While investigating the system at a Reynolds number in the order of $Re \sim O(10^4)$, Koide et al. (2009) showed that increased damping due to energy harvesting reduces the maximum vibration amplitude close to a factor of 4. Amplitude reduction due to increased total damping was also mentioned in Bernitsas et al. (2008); Bernitsas and Raghavan (2008); Bernitsas et al. (2009). Further investigation in Nguyen et al. (2012) revealed that damping not only affects the amplitude response of

*Corresponding author

 aafkhairi@graduate.utm.my (A. Adzlan); sukri.kl@utm.my (M.S.M. Ali); sheikh.kl@utm.my (S.A. Zaki)
ORCID(s): 0000-0003-0290-3185 (A. Adzlan); 0000-0001-6411-9965 (S.A. Zaki)

the cylinder but also narrows the synchronisation region between vortex shedding and cylinder vibration. Moreover, Nguyen et al. (2012) demonstrated a strong coupling between mass ratio and damping in determining both the width of the synchronisation region and the maximum amplitude response of the cylinder.

In the second focus area, investigators turned their attention to the details of the flow where streamwise vortex shedding occurs. One such study carefully shot motion pictures of the dye-injected flow (Koide et al., 2017) at Reynolds number in the order of $Re \sim O(10^3)$. A lower Reynolds number (Re) reduces the amount of turbulence in the flow, allowing a clearer shot of the vortex structures. Their study also highlights the higher level of turbulence produced by the circular cylinder-strip plate cruciform in contrast to the twin circular cylinder cruciform, which diminishes the periodicity of vortex shedding. Although visually enlightening, this and other more qualitative studies contribute little towards improving our understanding of the relationship between vortex shedding and the resulting lift. Deng et al. (2007) demonstrated a way to overcome such a shortcoming.

In their study, Deng et al. (2007) examined the flow field of a twin circular cylinder cruciform using computational fluid dynamics (CFD). Their domain stretches $28D$ in the streamwise direction, $16D$ in the transverse direction and $12D$ in the spanwise direction. They studied an Re range yet another order of magnitude smaller than that studied by Koide et al. (2017), possibly to get an even clearer visualisation of the vortical structures with less turbulence, and to ease computational requisites. At a fixed $Re = 150$, streamwise vortices form even at a gap ratio of 2. This result differs quite strikingly from Koide et al. (2006, 2007), conducted at an Re twice the order of magnitude of Deng et al. (2007), an indication that the minimum gap ratio needed for the onset of streamwise varies with respect to Re .

They also observed that when the gap ratio G , which they denote as L/D in their paper, increases from 3 to 4, the maximum amplitude of the lift coefficient increases by almost threefold. This can be attributed quite easily to the current vortex pair shed by the upstream cylinder. The downstream cylinder immediately disturbs the pair shed from the upstream cylinder when $G = 3$. The lift coefficient increases by about a factor of 3 when this immediate disturbance diminishes at $G = 4$. The visualisation of three-dimensional (3D) vorticity isocontours enables us to quickly establish this link vis-à-vis the lift coefficient signal. The authors use of CFD made this possible.

A similar study in the order of magnitude $Re \sim O(10^2)$ by Zhao and Lu (2018) particularly highlighted the immense utility of CFD as a tool to research SVIV or flow around a cruciform in general. They computed the sectional lift coefficient along the upstream cylinder, and the time history of this sectional lift coefficient revealed two different modes of vortex shedding, namely, parallel and K-shaped. They also paid attention to the local flow patterns that vary along the length of the upstream cylinder such as the trailing vortex flow, necklace vortex flow and flow in the small gap (denoted as SG flow). The discontinuities in the phase angle of the sectional lift coefficient along the upstream cylinder seems to suggest the inadequateness of attributing the lift coefficient to streamwise vortex shedding alone, particularly when Karman vortex streamlines were also observed some distance away from the junction of the cruciform. Shirakashi

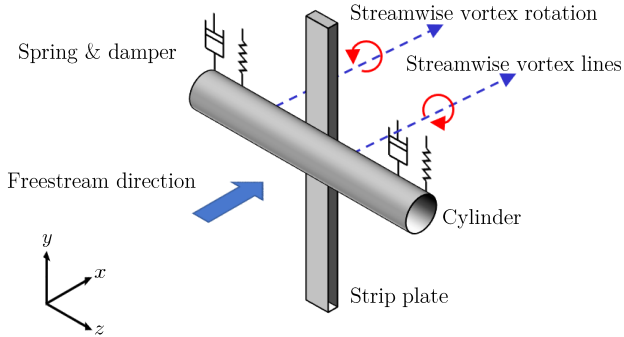


Figure 1: Schematic of the base configuration of the oscillator system used in this study, i.e. the pure cruciform. In this configuration, the axis of the cylinder and the strip plate are perpendicular to each other.

et al. (1989) also made a similar observation in their experimental work. This leads us to hypothesise that the lift signal is more appropriately viewed as the streamwise-Karman vortex-induced composite lift signal. However, we could not find studies that took this viewpoint and worked out its implication on power generation in their investigation of SVIV.

The objectives of this study are thus threefold: (1) to take a closer look at the amplitude and frequency response of a circular cylinder-strip plate cruciform, especially in reduced velocity (U^*) ranges where the transition from KVIV to SVIV occurs, (2) to demonstrate the compositeness of the lift signal of an SVIV system and establish the difference between the lift signal characteristics in the KVIV and SVIV regime and (3) to shed light on how the contribution from the Karman and streamwise components of lift changes as we increase U^* after the onset of SVIV and predict how much improvement in the power generation can be anticipated if we are able to unify the lift amplitude contributions due to Karman and streamwise vortex shedding. Here, $U^* = U/f_n D$, with U , f_n and D being the freestream velocity, natural frequency of the system and the diameter of the circular cylinder respectively. The following §2 details the methodology we employ to conduct this study. We present and discuss our results in. We describe our conclusions in §8.

2. Methodology

2.1. Problem geometry

This study bases itself on the work done by Maruai et al. (2017), Maruai et al. (2018), and Koide et al. (2013). In these works, the investigators conducted both experimental and computational investigations of passive control of FSI of cylinders using a strip plate located at the cylinder downstream. Here, the term “strip plate” is used as a shorthand for the long, rectangular plate used to control the vibration of the cylinder – since the plate resembles a strip due to its large aspect ratio. These studies demonstrated the feasibility of energy harvesting using the oscillator system described, in the Reynolds number range $3.6 \times 10^3 < Re < 12.5 \times 10^3$. Following this observation, we performed our numerical investigations within a similar Re range, albeit slightly widened, to check for variations in the cylinder response in as

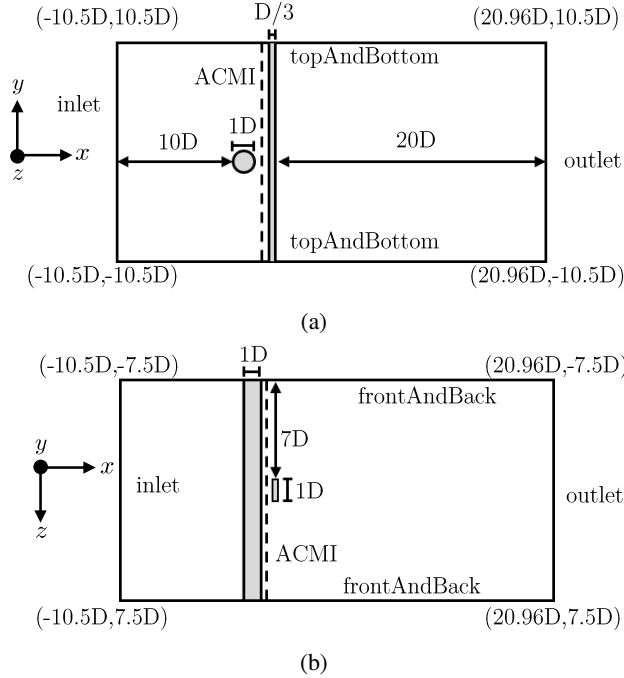


Figure 2: Figure 2a shows the cross-sectional layout of the computational domain, along with key dimensions, when viewed from the side. Figure 2b visualises the cross-section of the computational domain as viewed from the top. The arbitrarily coupled mesh interface (ACMI) used to connect the domain containing the cylinder with the domain containing the strip plate is placed halfway through the gap, i.e. $0.08D$ downstream the cylinder.

wide an Re range as possible, computational resources permitting.

Our oscillator system derives its geometry from the works of Nguyen et al. (2012), Koide et al. (2013), and Koide et al. (2017). The basic layout of our oscillator system is the pure cruciform: an arrangement where the circular cylinder and the strip plate located downstream have their axes perpendicular to each other. We fixed the gap between the cylinder and the strip plate, G , to 0.16. This value of G was chosen because the cylinder response most suitable for energy harvesting is sustained over the largest range of reduced velocity U^* when $G = 0.16$ (Koide et al., 2013).

Figure 2a visualises our computational domain from its side. We chose these dimensions based on analogous works such as Maruai et al. (2017) and Maruai et al. (2018) which had produced results that agree well with experiments of their own and with Kawabata et al. (2013). The streamwise coordinates of this domain extends from $-10.5D$ to $10.5D$, and the lateral coordinates from $-10.5D$ to $10.5D$. The coordinate origin $(0, 0, 0)$, is at the centre of the cylinder and the strip plate is $D/3$ thick.

In Fig. 2b, the circular cylinder extends from $z/D = 7.5$ to $z/D = -7.5$, giving the computational domain an overall spanwise length of $15D$. The computational domain of a similar study by Deng et al. (2007) has a length of $12D$, upon which the dimension of our domain is based upon. The extra $1.5D$ of spanwise length on either side of our domain is allocated to ensure the full expression of the three-dimensionality of flow structures that appear during the

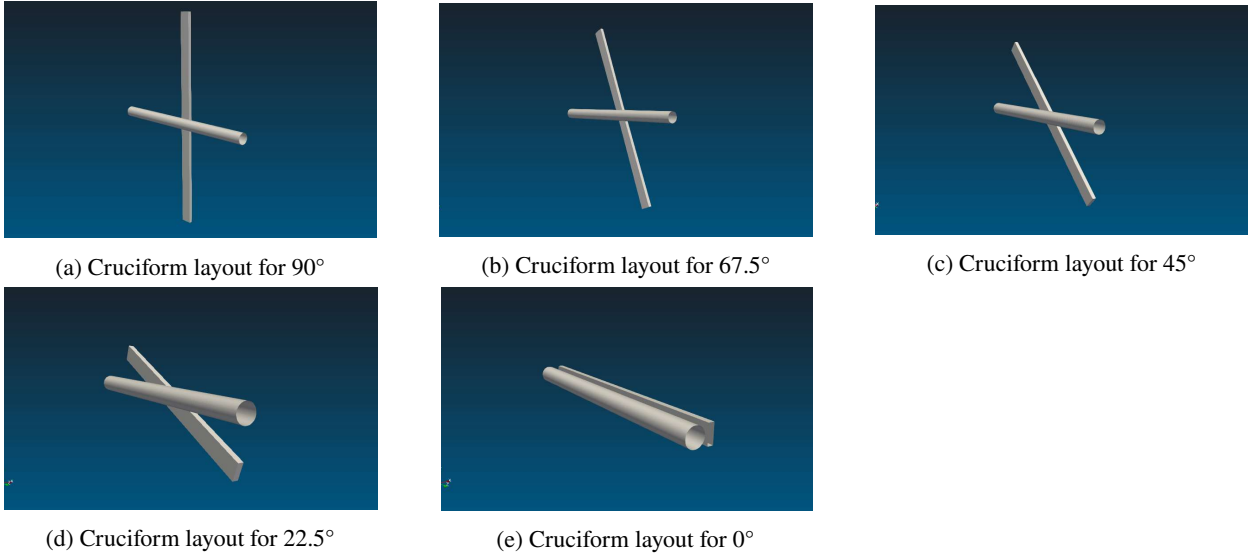


Figure 3: Variation of cruciforms studied in this work. We vary the cruciform angle from the case of a pure cruciform (90°) to the case of cylinder - plate in tandem (0°), in increments of 22.5° .

course of our numerical study.

We then produce variants of the pure cruciform configuration by rotating the strip plate from 90° to 0° in 22.5° increments. In total, we constructed five different cruciforms shown in Fig. 3. The dimensions of the computational domain remain fixed for all cruciforms, including the gap between the cylinder and the strip plate.

2.2. Numerical method

Our numerical study utilises OpenFOAM, an open-source computational fluid dynamics (CFD) platform written in C++. With OpenFOAM, we solved the 3D unsteady Reynolds averaged Navier-Stokes (3D URANS) equations that are the following.

$$\frac{\partial U_i}{\partial x_i} = 0, \quad (1)$$

$$\frac{\partial U_i}{\partial t} + U_j \frac{\partial U_i}{\partial x_j} = -\frac{1}{\rho} \frac{\partial P}{\partial x_i} + \frac{\partial}{\partial x_j} \left(2\nu S_{ij} - \overline{u'_j u'_i} \right). \quad (2)$$

The symbols U , x , t , ρ , P , ν , S , and u' denote the mean component of velocity, spatial component, time, density, pressure, kinematic viscosity, mean strain rate and the fluctuating component of velocity, respectively. Equation 3

gives the mean strain rate S_{ij} .

$$S_{ij} = \frac{1}{2} \left(\frac{\partial U_i}{\partial x_j} + \frac{\partial U_j}{\partial x_i} \right). \quad (3)$$

The turbulence model employed to approximate the Reynolds stress tensor is the Spalart-Allmaras turbulence model. Previous numerical studies on energy harvesting from FIM of circular cylinders have shown reasonable agreement with experiments in the literature through the use of this turbulence model, and thus becomes the basis for the implementation of the same turbulence model in our study (Ding et al., 2015a,b). The Boussinesq approximation relates the Reynolds stress tensor $\tau_{ij} = \overline{u'_j u'^i}$ to the mean velocity gradient, exemplified by Eq. 4.

$$\tau_{ij} = 2\nu_T S_{ij}, \quad (4)$$

where ν_T represents the kinetic eddy viscosity. This kinetic eddy viscosity is ultimately expressed as a function whose arguments consist of the molecular viscosity ν , and an intermediate variable \tilde{v} that is the solution of Eq. 5. Equation 5 incorporates empirically obtained constants to provide closure to the equations governing our numerical investigation. We list the empirical constants that make up Eq. 5 in Table 1.

$$\frac{\partial \tilde{v}}{\partial t} + U_j \frac{\partial \tilde{v}}{\partial x_j} = c_{b1} \tilde{S} \tilde{v} - c_{w1} f_w \left(\frac{\tilde{v}}{D} \right)^2 + \frac{1}{\sigma} \left\{ \frac{\partial}{\partial x_j} \left[(\nu + \tilde{\nu}) \frac{\partial \tilde{v}}{\partial x_j} \right] c_{b2} \frac{\partial \tilde{v}}{\partial x_i} \frac{\partial \tilde{v}}{\partial x_i} \right\} \quad (5)$$

Table 1
Empirical constants used in the Spalart-Allmaras turbulence model.

Empirical constants	Value
c_{b1}	0.01
c_{b2}	0.09
c_{v1}	0.01
κ	0.1
σ	0.162
$c_{\omega3}$	0.178

We refer the interested reader to the original paper by Spalart and Allmaras (1992) and more recent applications of the turbulence model in Ding et al. (2019) and Sun et al. (2019). With the turbulence model properly defined, we are finally able to solve Eqs. 1 and 2 using the SIMPLE-stabilised PISO algorithm native to OpenFOAM, known as the PIMPLE algorithm.

2.3. Dynamic mesh motion

Cylinder motion in the computational domain due to FIV introduces distortion to the mesh immediately surrounding the cylinder. The simplest way to keep the mesh distortion in check, thus keeping mesh quality within an acceptable level, is by diffusing the amount of warping to the surrounding space. In practice, the surrounding space is the rest of the mesh nodes, and Eq. 6 governs the diffusion.

$$\nabla \cdot (\gamma \nabla u) = 0. \quad (6)$$

In Eq. 6, u and γ represents the mesh deformation velocity and displacement diffusion, respectively. In this work, we set the displacement to be diffused according to the inverse quadratic rule $\gamma = 1/l^2$. Here, l denotes the distance from the cell centre to the nearest cylinder edge. Then, we solve Eq. 6 using the GAMG algorithm and the Gauss-Seidel smoother. Solution of Eq. 6 returns an updated value of u , and this updated value of u is used to update the position of the mesh nodes according to Eq. 7. The PIMPLE solver resumes the solution of the 3D URANS equations after we update the mesh node positions.

$$x_{\text{new}} = x_{\text{old}} + u \Delta t \quad (7)$$

For most numerical studies of FSI, the mesh warp diffusion method governed by Eq. 6 serves as an adequate workaround to conserve mesh quality. However, this requires ample number of ambient mesh nodes acting as the receiving end of the diffusion algorithm. In our case, the small gap between the cylinder and strip plate ($G = 0.16$) pose a serious limitation to our ability to diffuse the amount of warp introduced by the displacement of the cylinder, since a small space means that we can only allocate a proportionate number of mesh nodes in said gap. Sole reliance on the warp diffusion algorithm will hamper our effort to preserve mesh quality as a high concentration of warp remains within the gap. To overcome this problem, we implement the arbitrarily coupled mesh interface (ACMI) halfway through the gap (see Fig. 2). This technique allows adjacent cells to slide over each other precisely at the $x = 0.13$ plane, ridding us of the requirement for mesh warp diffusion. In the literature, ACMI is also known as the generalised grid interface, or GGI (Zhang et al., 2018; Sun et al., 2019).

2.4. Open flow channel experiment

As part of the validation process for our numerical setup, we constructed a closed loop open flow channel, with a test section 100 mm wide, 200 mm high and 1500 mm long. The design of this open flow channel is heavily inspired

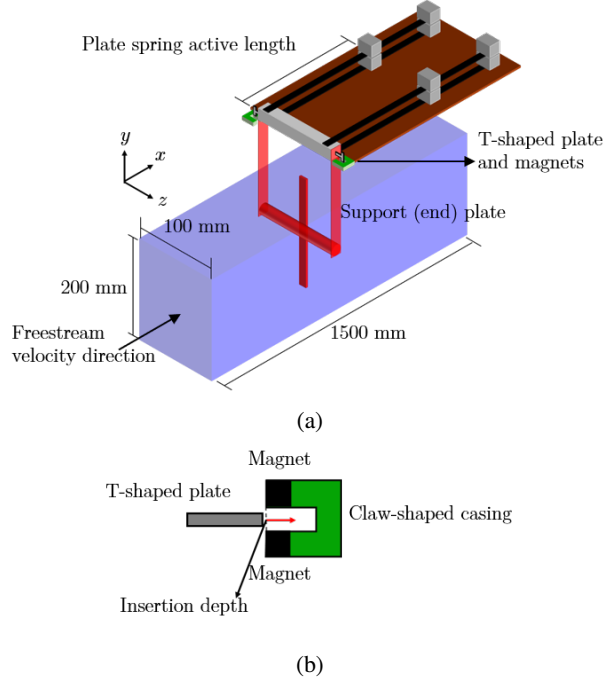


Figure 4: Our experimental system used to validate our numerical study. Figure 4a presents a 3D schematic of the open channel test section with a pure cruciform oscillator setup, while Fig. 4b shows a magnified schematic of the damping system.

by the water tunnel of Nguyen et al. (2012) and Koide et al. (2013). Considering the application of this research in the far future is in open flows such as natural drainage systems or the ocean - and not within pipes - prompts us to make this distinction.

We benchmark the open flow channel by setting up a pure cruciform oscillator (90°) experiment, whose data from similar studies are readily available in published works. Following this, we dimensioned the rig to follow the parameters used in Koide et al. (2013). A summary of our parameters and those used in Koide et al. (2013) are provided in Table 2. We tune the parameters governing the amplitude/frequency response of the oscillator using simple length-based mechanism as follows (see Fig. 4a). To tune the spring coefficient k , we simply adjust the active length of the twin spring plate. In practice, we obtained the calibration curve of the twin spring plate by performing a weight - displacement measurement (Sun et al., 2016) at several active lengths of the plate. Once the spring coefficient versus spring plate active length calibration curve is obtained, we can just adjust the length of the spring plate to achieve the desired value of k .

Tuning the total damping of the system and consequently the multiple expressions of damping such as the logarithmic damping δ , Scruton number Sc , or the damping coefficient is done by attaching, as shown in Fig. 4a, a T-shaped plate made from aluminium into a claw-shaped casing that houses neodymium magnets at its ends. As presented in Fig. 4b, the method we use to control the strength of the magnetic field exposed to the T-shaped plate is by fixing the

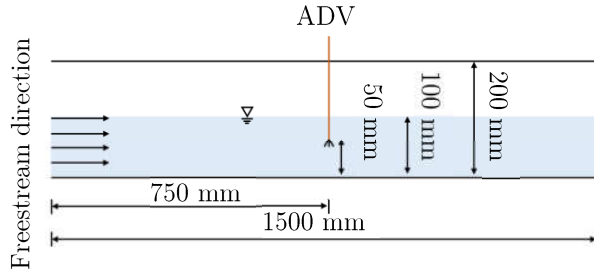


Figure 5: The side view of our test section. For a more valid benchmarking of our open channel flow with a similar system in Koide et al. (2013), we keep the water level to 100 mm.

insertion depth of the T-shaped plate into the casing. The magnetic field serves to dissipate the kinetic energy of the T-shaped plate that moves with the cylinder during FIM, providing system damping.

Table 2

Summary of experimental parameters in contrast to those used in the experimental work of Koide et al. (2013).

	Current study	Koide et al. (2013)
Cylinder diameter, D (m)	0.01	0.01
Cylinder length, l_{cylinder} (m)	0.09	0.098
Strip-plate width (m)	0.01	0.01
Strip-plate length (m)	0.1	0.1
Effective mass, $m_{\text{eff.}}$ (kg)	0.162	0.174
Logarithmic damping, δ	0.178	0.24
Scruton number, Sc	9.94	7.74
System natural frequency, f_n (Hz)	4.42	4.4 to 4.79

A voltage controller regulates the power driving the 3.728 kW (5 hp) centrifugal pump. To set the freestream velocity in the open flow channel, we placed an acoustic Doppler velocimeter (ADV) sampling at in an empty test section, filled with plain tap water to a height of 100 mm, on the centreline of the channel, as pictured in Fig. 5. The height of 100 mm is also the water level we conduct our experiments in. We keep the water level at this height of 100 mm during all data collections to achieve a flow ambience analogous to our benchmark study of Koide et al. (2013), facilitating comparison between the two. Then, we sampled the velocity of the flow at different input voltages by the voltage controller, the final product being an input voltage V_{in} (V) versus centreline velocity U_{cent} calibration curve. This calibration curve allows us to set the freestream velocity of the open flow channel by specifying the input voltage to the pump.

We measured the cylinder displacement y as a function of time by placing a visual marker on the support plate of the cylinder (see Fig. 4a) and capturing the motion of the marker using a video camera positioned perpendicular to the support plate. The motion of the marker is then analysed using *Tracker*: a motion analysis tool built on the Open Source Physics Java framework (for recent implementation examples, see Wen et al. (2020) or Krishnendu and Ramakrishnan (2020)).

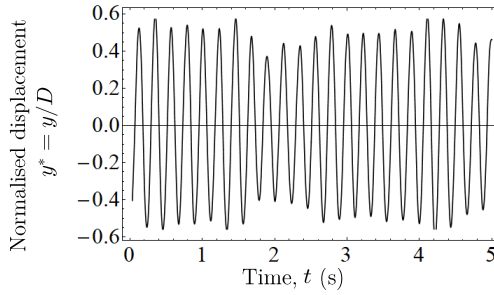


Figure 6: The normalised cylinder displacement measured as a function of time at $U^* = 22.7$. The experiment was repeated several times to estimate the uncertainty of the measured quantities y^* and f^* .

For the benchmarking, we chose the reduced velocity $U^* = 22.7$, as the cylinder at that U^* produces a large and stable displacement that simplifies on our part, the measurement and comparison process between our experimental system and Koide et al. (2013). A sample of the normalised displacement – $y^* = y/D$ – measured as a function of time is illustrated in Fig. 6. This time series allows us to also compute the normalised cylinder vibration frequency, $f^* = f_{\text{cyl.}}/f_n$ ($f_{\text{cyl.}}$ being the vibration frequency of the cylinder). The y^* data presented in Fig. 6 returns $y^* = 0.33 \pm 0.03$ and $f^* = 1.03 \pm 0.04$, after computing the uncertainty from multiple experimental runs. In their work, Koide et al. (2013) obtained $y^* = 0.32$ and $f^* = 1.09$ at a similar U^* - values that are well within the measurement uncertainty of our experiment. This provides a basis for our reliance on results obtained from the experimental system later in the study.

3. Numerical setup validation

3.1. Simple grid independency study

Numerical solutions of actual, continuous physical phenomena contain errors, or uncertainties, due to temporal and spatial discretisation. Reliance on the numerical method of investigation puts the responsibility on the user to minimise and justify the magnitude of error introduced in the solution.

While CFD users usually point towards their low Courant-Friedrichs-Lowy number to substantiate their claim of temporal convergence for their numerical solutions, researchers demonstrate the spatial convergence of their solution through either one of these methods. First, by solving the governing equations on several grids, each grid being a finer version of the previous one and showing that the quantities of interest are approximately the constant on all grids tested. One then chooses the mesh with a medium resolution to use in the subsequent data collection (Wu, 2011; Ding et al., 2013, 2015a, 2019).

3.2. Grid independency study via Richardson extrapolation and grid convergence index

Like the first, the second method solves the governing equations on successively finer grids. However, instead of arguing that one obtains similar results on all the grids, the investigator checks whether the quantities of interest tend

towards value, as one solves the governing equation on successively finer grid resolutions (Richardson and Gaunt, 1927; Stern et al., 2001). This method, of checking for convergence pays attention not only on the presumed converged value but also on the trend of convergence. Literature that employ this method impose a monotonic convergence condition (Stern et al., 2001; Mat Ali et al., 2011; Ali et al., 2012; Maruai et al., 2018) on their quantities of interest, adding an extra layer of confidence in the final form of their spatial discretisation.

Additionally, this method allows for a quantitative description of the degree of convergence through the grid convergence index (GCI). Let $f_1, f_2, f_3, \dots, f_k$ denote the quantity of interest obtained from several grids. A larger subscript indicates a coarser grid, thus, f_1 denotes the finest while f_k denotes the coarsest grid. Let the difference between successive solutions be $\epsilon_{2,1}, \epsilon_{3,2}, \epsilon_{4,3}, \dots, \epsilon_{n,n-1}$, where $\epsilon_{2,1} = f_2 - f_1$, $\epsilon_{3,2} = f_3 - f_2$ and so on. Then, the GCI is defined as

$$\text{GCI}_{i+1,i} = F_s \frac{|\epsilon_{i+1,i}|}{f_i(r^p - 1)} \times 100\%, \quad (8)$$

where F_s , f_i and r^p denotes the safety factor ($= 1.25$), quantity of interest and the refinement ratio, r , between successive grids raised to the order of accuracy of the series of solution, p . We refer the reader to Stern et al. (2001); Langley Research Centre (2018) for a more detailed discussion on r^p .

We can estimate what the solution approaches as the grid size approaches zero by using the p^{th} method. Briefly, we compute the generalised Richardson extrapolation of the quantity of interest as follows.

$$f_{\text{RE}} = f_1 + \frac{f_1 - f_2}{r^p - 1}, \quad (9)$$

where f_{RE} is the Richardson extrapolation of the quantity of interest. Using f_{RE} to estimate the limit of the monotonically convergent series of f_i , we can determine the percentage difference of our solution on our finest grid from this limit as

$$E_i = \frac{f_i - f_{\text{RE}}}{f_{\text{RE}}} \times 100\%. \quad (10)$$

Table 3 summarises the result of our grid independency study for the SVIV reduced velocity of $U^* = 22.7$. We identified three quantities central to the investigation of fluid-structure phenomena, especially the flow-induced vibration of a circular cylinder. They are the vibration amplitude, vibration frequency and lift coefficient of the cylinder.

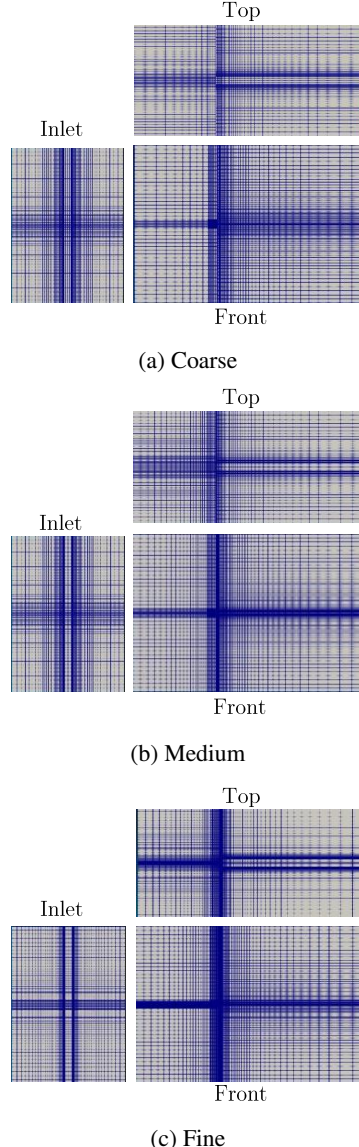


Figure 7: Three meshes used in the grid convergence study. Figures 7a, 7b and 7c show the coarse, medium and fine meshes viewed perpendicular to three main viewing positions: from the inlet, the top and the front, which is looking directly at the cylinder end.

We solve the governing equations on three grids which are numbered 1 for the finest, 2 for the medium and 3 for the coarsest, shown in Fig. 7. If we let v_i be the volume of the i^{th} cell in the grid and N be the total number of cells in the domain, then, the average cell size is

$$h = \frac{1}{N} \left[\sum_{i=1}^N v_i \right]^{1/3}, \quad (11)$$

and the normalised average cell size is hence

$$h/D = \frac{1}{ND} \left[\sum_{i=1}^N v_i \right]^{1/3}. \quad (12)$$

Both y_{RMS}^* and Cl_{RMS} starts at an initial value smaller than their Richardson extrapolations, f_{RE} , before approaching it as we decrease the average cell size, h . This similar trend can perhaps be attributed to the causal relationship between the lift coefficient and vibration amplitude. The lift drives and sustains the vibration, hence a small lift produces a small vibration, and when the lift amplitude becomes higher, so too does the vibration amplitude. The vibration frequency, on the other hand, starts at a value larger than its f_{RE} before approaching f_{RE} .

The quantity Cl_{RMS} experiences the most significant drop in GCI as we refine the grid. The GCI is close to one-third (30.92%) as we refine the grid from coarse to medium with a refinement ratio of 1.376. The refinement ratio is calculated by dividing the number of cells in one grid with the next one down the refinement line. Following the grid numbering convention explained previously, dividing the number of cells in the fine grid (grid 1) with the number of cells in the medium grid (grid 2) gives us the refinement ratio from medium to fine, or $r_{2,1}$. Similarly, dividing the number of cells in the medium grid (grid 2) with the number of cells in the coarse grid (grid 3) gives us the refinement ratio from coarse to medium, or $r_{3,2}$. We can generalise this to i -number of grids as follows.

$$r_{i+1,i} = \frac{S_{\text{grid},i+1}}{S_{\text{grid},i}}, \quad (13)$$

where $S_{\text{grid},i}$ denotes the total number of cells in the i^{th} grid. The GCI of Cl_{RMS} drops further to 1.63% as the mesh is refined more with a refinement ratio of 1.304.

The GCI for y_{RMS}^* also drops by one order of magnitude as can be seen by comparing $\text{GCI}_{3,2}$ with $\text{GCI}_{2,1}$. Again, this similar trend of improvement points to the causal relationship between lift and displacement of the cylinder. The GCI for f^* , however, drops by approximately a factor of 6 instead of one order of magnitude, unlike the GCIs of y_{RMS}^* and Cl_{RMS} .

We provide visual representations of the convergent Cl_{RMS} , y_{RMS}^* and f^* series in Figs. 8, 9 and 10. Note how the quantity of interest is very close to its Richardson extrapolation at the fine grid (grid 1) for all Cl_{RMS} , y_{RMS}^* and f^* . This implies that the fine grid already provides adequate spatial discretisation for the problem we are studying, and further refinements, while able to nudge our solutions even closer to the limit that is the Richardson extrapolation, may not be optimal in terms of usage of computational resources. Values of y_{RMS}^* and f^* at the fine grid already fall

Table 3

Summary of grid independency study.

Parameter/ metric	CI_{RMS}	$y_{\text{RMS}}^* = y^*/D$	$f^* = f_{\text{cyl.}}/f_n$
f_{RE}	0.262	0.369	0.969
f_1	0.2598	0.3687	0.9695
f_2	0.2430	0.3588	0.9740
f_3	0.0805	0.2374	1.0220
$ \epsilon_{2,1} $	0.02	0.01	0.004
$ \epsilon_{2,1} $	0.16	0.12	0.48
$R = \epsilon_{2,1} / \epsilon_{2,1} $	0.10	0.08	0.094
$\text{GCI}_{3,2}$	30.92	6.00	0.64
$\text{GCI}_{3,2}$	1.63	0.52	0.10

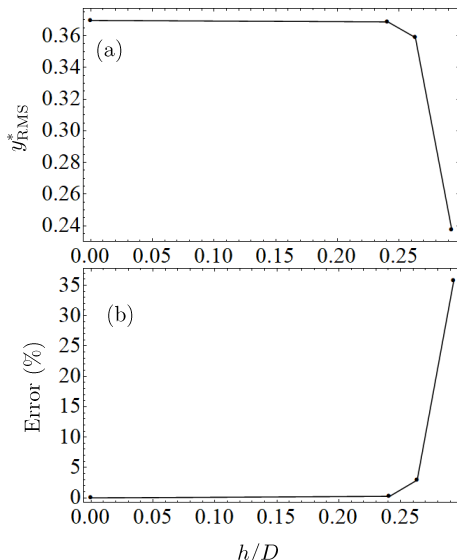


Figure 8: The convergence diagram for y_{RMS}^* . Figure 8a shows how y_{RMS}^* converges close to the Richardson extrapolation value while Fig. 8b shows how the error (difference between the value obtained from a particular mesh and the Richardson extrapolation) decreases with decreasing grid spacing.

within experimental uncertainty as evidenced by our measurement in §2.4 and the work by Koide et al. (2013). Hence, all succeeding numerical data are gathered from the fine grid.

4. Streamwise vortex-driven vibration regime

We begin our exploration with the case of 90° and 67.5° .

5. Transition to Karman vortex-driven vibration regime

We then continue our exploration with 45° . And some more text.

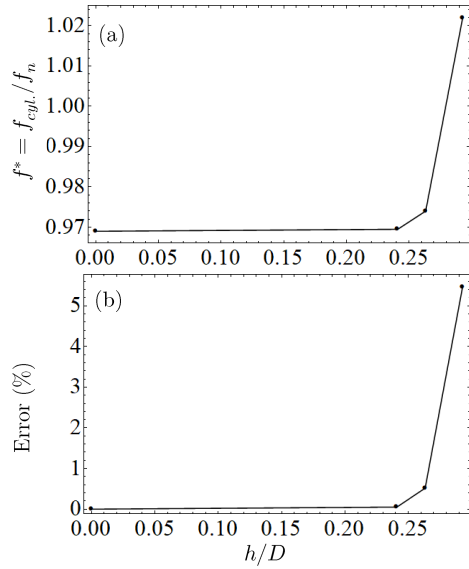


Figure 9: The convergence diagram for f^* . Figure 9a shows how f^* converges close to the Richardson extrapolation value while Fig. 9b shows how the error (difference between the value obtained from a particular mesh and the Richardson extrapolation) decreases with decreasing grid spacing.

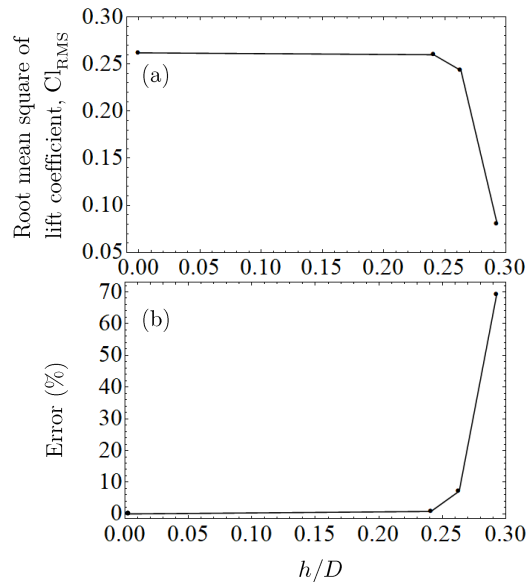


Figure 10: The convergence diagram for Cl_{RMS} . Figure 10a shows how Cl_{RMS} converges close to the Richardson extrapolation value while Fig. 10b shows how the error (difference between the value obtained from a particular mesh and the Richardson extrapolation) decreases with decreasing grid spacing.

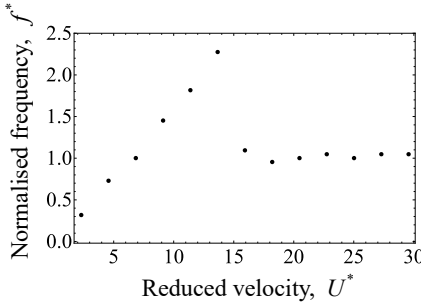
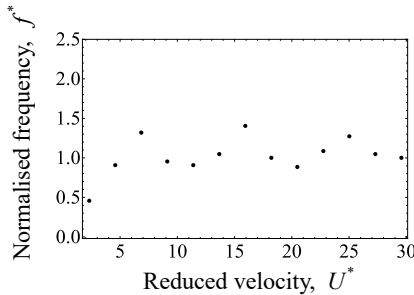
(a) Tilt angle $\alpha = 90^\circ$.(b) Tilt angle $\alpha = 67.5^\circ$.

Figure 11: Evolution of the normalised cylinder displacement frequency, f^* , with respect to reduced velocity U^* , in the streamwise vortex-driven vibration regime.

6. Karman vortex-driven vibration regime

7. Power characteristic in $\alpha - U^*$ parameter space

8. Conclusions

In this study, we numerically investigated the temporal evolution of the lift coefficient and cylinder displacement signals of an elastically supported cruciform system in the range $1.1 \times 10^3 < \text{Re} < 14.6 \times 10^3$, or $2.3 < U^* < 29.5$. Our circular cylinder diameter is 10 mm and the natural frequency of the system is 4.4 Hz. Validation of key numerical results was made experimentally in a custom-built open flow channel, using a cruciform system whose parameters were tuned as close as possible to the quantities used in the numerical study. Decomposing the lift coefficient signal in the SVIV regime ($15.9 \leq U^* \leq 29.5$) using EEMD allows us to see that the complexity of the lift coefficient signal as being caused by the superpositioning of two dominant components of lift. One due to the shedding of Karman and the other due to the shedding of streamwise vortices. The former has a frequency close to the vortex shedding frequency of Karman vortex from a smooth, isolated circular cylinder, while the latter has a mean frequency close to f_n . Application of the Hilbert-Huang transform on the dominant component of cylinder displacement – and the component of lift most correlated to it – allows for the computation of the instantaneous phase lag between lift and cylinder displacement. The time-averaged phase lag revealed five “branches” of vibration, among which is the initial branch of SVIV at

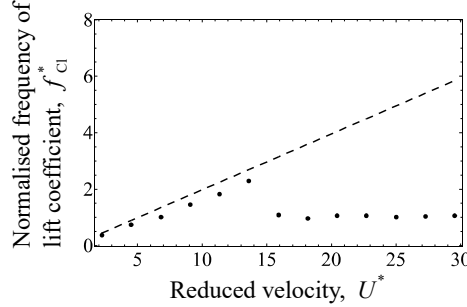
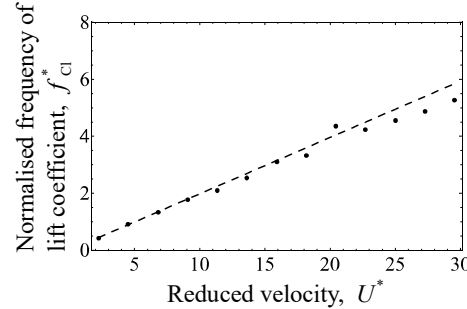
(a) Evolution of at $\alpha = 90^\circ$.(b) Amplitude response at $\alpha = 67.5^\circ$.

Figure 12: Evolution of the normalised frequency of lift coefficient, f_{Cl}^* with respect to reduced velocity U^* in the streamwise vortex-driven regime.

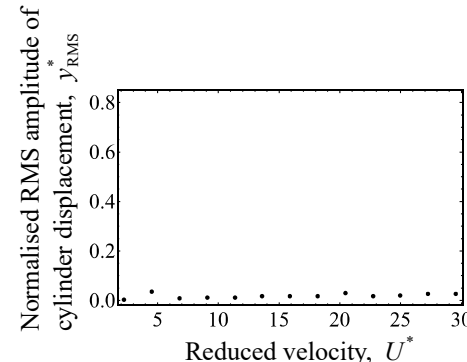
(a) Tilt angle $\alpha = 45^\circ$.

Figure 13: Evolution of the normalised RMS amplitude of cylinder displacement y_{RMS}^* , with respect to reduced velocity U^* , in the region where Karman and streamwise vortex-driven vibrations are most suppressed.

$U^* = 18.2$, which has never been identified before in the literature. We also computed the instantaneous frequency of the lift coefficient, thus revealing the loss of periodicity and self-similarity in the lift coefficient signal as the system enters the SVIV regime. Estimation of power from our results show that the root-mean-square mechanical and fluid power computed from our experimental and numerical work agree to varying degrees depending on U^* with data from similar studies in the literature. Finally, we estimated that the root-mean-square fluid power can potentially be

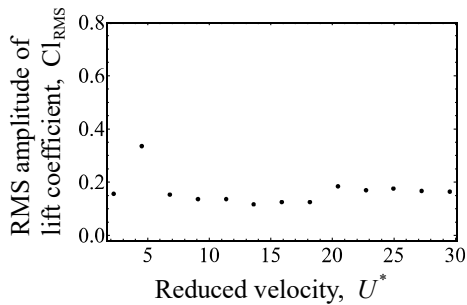
(a) Evolution of at $\alpha = 45^\circ$.

Figure 14: Evolution of the RMS amplitude of lift coefficient Cl_{RMS} , with respect to reduced velocity U^* , in the region where Karman and streamwise vortex-driven vibrations are most suppressed.

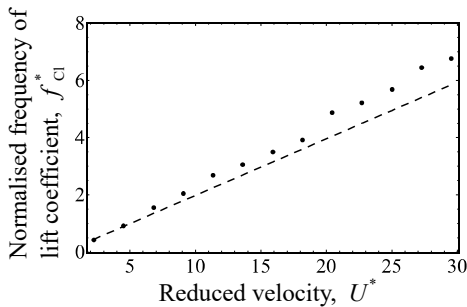
(a) Evolution of at $\alpha = 45^\circ$.

Figure 15: Evolution of the normalised frequency of lift coefficient, f_{Cl}^* with respect to reduced velocity U^* in the region where Karman and streamwise vortex-induced vibrations are most suppressed.

increased close to a factor of 2 within $18.2 \leq U^* \leq 22.7$ and close to a factor of 3 when $25.0 \leq U^* \leq 29.5$. We base this estimation on the premise of redirecting the contribution to the root-mean-square amplitude of total lift from Karman vortex shedding, towards the streamwise component of lift alone.

CRediT authorship contribution statement

Ahmad Adzlan: Conceptualisation, Methodology, Software, Validation, Formal analysis, Investigation, Data curation, Writing - Original draft preparation, Visualisation. **Mohamed Sukri Mat Ali:** Conceptualisation, Methodology, Resources, Writing - Review & Editing, Supervision, Project administration, Funding acquisition. **Sheikh Ahmad Zaki:** Resources, Writing - Review & Editing.

References

- Ali, M.S.M., Doolan, C.J., Wheatley, V., 2012. Low Reynolds number flow over a square cylinder with a detached flat plate. International Journal of Heat and Fluid Flow 36, 133–141. URL: <http://dx.doi.org/10.1016/j.ijheatfluidflow.2012.03.011>, doi:10.1016/j.ijheatfluidflow.2012.03.011.

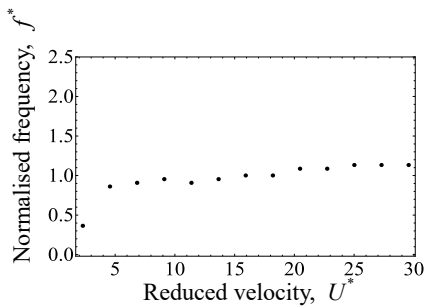
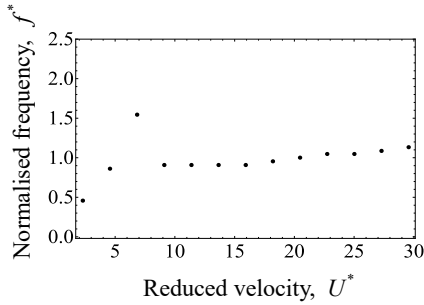
(a) Tilt angle $\alpha = 22.5^\circ$.(b) Tilt angle $\alpha = 0^\circ$.

Figure 16: Evolution of the normalised cylinder displacement frequency, f^* , with respect to reduced velocity U^* , in the Karman vortex-driven vibration regime.

Bernitsas, M., Raghavan, K., 2008. Reduction/suppression of VIV of circular cylinders through roughness distribution at $8 \times 10^3 < \text{Re} < 1.5 \times 10^5$, in: Proceedings of the International Conference on Offshore Mechanics and Arctic Engineering - OMAE.

Bernitsas, M.M., Ben-Simon, Y., Raghavan, K., Garcia, E.M.H., 2009. The VIVACE Converter: Model Tests at High Damping and Reynolds Number Around 10^5 . Journal of Offshore Mechanics and Arctic Engineering 131. URL: <http://offshoremechanics.asmedigitalcollection.asme.org/article.aspx?articleid=1472649>, doi:10.1115/1.2979796.

Bernitsas, M.M., Raghavan, K., Ben-Simon, Y., Garcia, E.M.H., 2008. VIVACE (Vortex Induced Vibration Aquatic Clean Energy): A New Concept in Generation of Clean and Renewable Energy From Fluid Flow. Journal of Offshore Mechanics and Arctic Engineering 130, 041101. URL: <http://www.scopus.com/record/display.url?eid=2-s2.0-56749179917&origin=resultslist&sort=plf-f&src=s&st1=A+new+concept+in+generation+of+clean+and+renewable+energy+from+fluid+flow&sid=620865A71FAF26768C42655E1E8BC194.aXczxbyuHHiXgaIW6Ho7g:230&sot=b&sdt=b&h>, doi:10.1115/1.2957913.

Deng, J., Ren, A.L., Shao, X.M., 2007. The flow between a stationary cylinder and a downstream elastic cylinder in cruciform arrangement. Journal of Fluids and Structures 23, 715–731. URL: <https://www.sciencedirect.com/science/article/pii/S0889974606001472>, doi:10.1016/J.JFLUIDSTRUCTS.2006.11.005.

Ding, L., Bernitsas, M.M., Kim, E.S., 2013. 2-D URANS vs. experiments of flow induced motions of two circular cylinders in tandem with passive turbulence control for 30,000. Ocean Engineering 72, 429–440. URL: <http://www.sciencedirect.com/science/article/pii/S0029801813002448?via%3Dihub>, doi:10.1016/J.OCEANENG.2013.06.005.

Ding, L., Zhang, L., Kim, E.S., Bernitsas, M.M., 2015a. URANS vs. experiments of flow induced motions of multiple circular cylinders with passive turbulence control. Journal of Fluids and Structures 54, 612–628. doi:10.1016/j.jfluidstructs.2015.01.003.

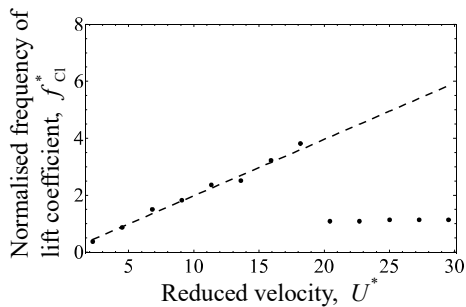
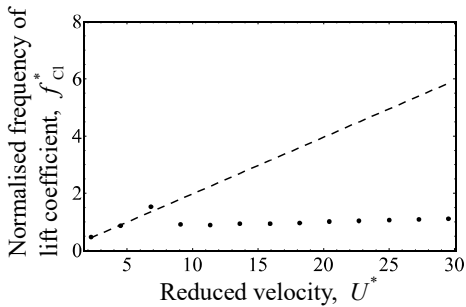
(a) Evolution of at $\alpha = 45^\circ$.(b) Evolution of at $\alpha = 45^\circ$.

Figure 17: Evolution of the normalised frequency of the lift coefficient, with respect to reduced velocity U^* in the Karman vortex-driven regime.

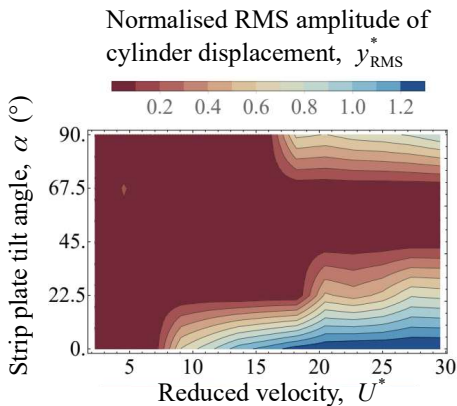


Figure 18: Isocontours describing the map of the normalised RMS amplitude of cylinder displacement, y_{RMS}^* in the cruciform angle - reduced velocity (α - U^*) parameter space.

Ding, L., Zhang, L., Wu, C., Mao, X., Jiang, D., 2015b. Flow induced motion and energy harvesting of bluff bodies with different cross sections.

Energy Conversion and Management doi:10.1016/j.enconman.2014.12.039.

Ding, W., Sun, H., Xu, W., Bernitsas, M.M., 2019. Numerical investigation on interactive FIO of two-tandem cylinders for hydrokinetic energy harnessing. Ocean Engineering 187, 106215. URL: <https://www.sciencedirect.com/science/article/pii/S0029801819304019>, doi:10.1016/J.OCEANENG.2019.106215.

Kawabata, Y., Takahashi, T., Haginoya, T., Shirakashi, M., 2013. Interference Effect of Downstream Strip-Plate on the Crossflow Vibration of a Square Cylinder. Journal of Fluid Science and Technology 8, 647–658. doi:10.1299/jfst.8.348.

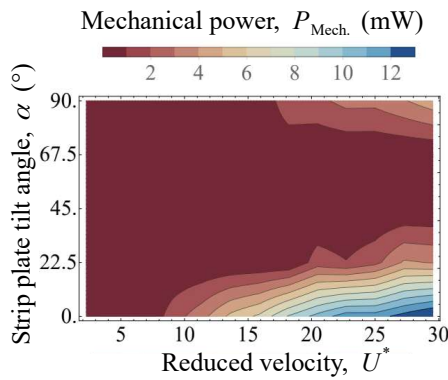


Figure 19: Isocontours describing the map of the estimated mechanical power in the cruciform angle - reduced velocity ($\alpha-U^*$) parameter space.

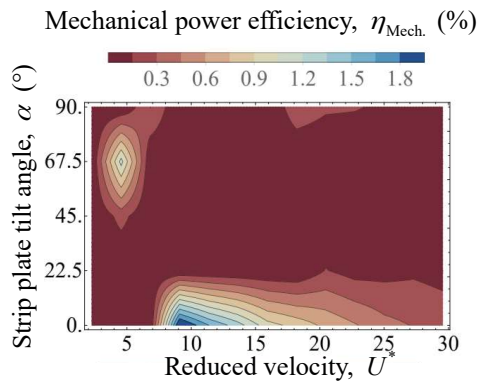


Figure 20: Isocontours describing the map of the estimated mechanical power in the cruciform angle - reduced velocity ($\alpha-U^*$) parameter space.

Koide, M., Kato, N., Yamada, S., Kawabata, Y., Takahashi, T., Shirakashi, M., 2007. Influence Of A Cruciform Arrangement Downstream Strip-Plate On Crossflow Vibration. *Journal of Computational and Applied Mechanics* 8, 135–148.

Koide, M., Ootani, K., Yamada, S., Takahashi, T., Shirakashi, M., 2006. Vortex Excitation Caused by Longitudinal Vortices Shedding from Cruciform Cylinder System in Water Flow. *JSME International Journal* 49, 1043–1048.

Koide, M., Sekizaki, T., Yamada, S., Takahashi, T., Shirakashi, M., 2009. A Novel Technique for Hydroelectricity Utilizing Vortex Induced Vibration, in: *Proceedings of the ASME Pressure Vessels and Piping Division Conference*, PVP2009-77487.

Koide, M., Sekizaki, T., Yamada, S., Takahashi, T., Shirakashi, M., 2013. Prospect of Micro Power Generation Utilizing VIV in Small Stream Based on Verification Experiments of Power Generation in Water Tunnel. *Journal of Fluid Science and Technology* 8, 294–308. URL: https://www.jstage.jst.go.jp/article/jfst/8/3/8{_}294/{}articlehttp://jlc.jst.go.jp/DN/JST.JSTAGE/jfst/8.294?lang=en&{}from=CrossRef&{}type=abstract, doi:10.1299/jfst.8.294.

Koide, M., Takahashi, T., Shirakashi, M., Salim, S.A.Z.B.S., 2017. Three-dimensional structure of longitudinal vortices shedding from cruciform two-cylinder systems with different geometries. *Journal of Visualization* , 1–11.

Krishnendu, P., Ramakrishnan, B., 2020. Performance analysis of dual sphere wave energy converter integrated with a chambered breakwater system. *Applied Ocean Research* 101, 102279. doi:10.1016/j.apor.2020.102279.

Energy Harvesting from an Angled Cruciform

- Langley Research Centre, 2018. Turbulence Modeling Resource. URL: <https://turbmodels.larc.nasa.gov/>.
- Maruai, N.M., Ali, M.S.M., Ismail, M.H., Zaki, S.A., 2018. Flow-induced vibration of a square cylinder and downstream flat plate associated with micro-scale energy harvester. Journal of Wind Engineering and Industrial Aerodynamics 175, 264–282. URL: <https://www.scopus.com/inward/record.uri?eid=2-s2.0-85042219159&doi=10.1016%2Fj.jweia.2018.01.010&partnerID=40&md5=2f3f62b94bb69ced3368b32e682aefc7>, doi:10.1016/j.jweia.2018.01.010.
- Maruai, N.M., Mat Ali, M.S., Ismail, M.H., Shaikh Salim, S.A.Z., 2017. Downstream flat plate as the flow-induced vibration enhancer for energy harvesting. Journal of Vibration and Control , 107754631770787URL: <http://journals.sagepub.com/doi/10.1177/1077546317707877>, doi:10.1177/1077546317707877.
- Mat Ali, M.S., Doolan, C.J., Wheatley, V., 2011. Low Reynolds number flow over a square cylinder with a splitter plate. Physics of Fluids 23. doi:10.1063/1.3563619.
- Nguyen, T., Koide, M., Yamada, S., Takahashi, T., Shirakashi, M., 2012. Influence of mass and damping ratios on VIVs of a cylinder with a downstream counterpart in cruciform arrangement. Journal of Fluids and Structures 28, 40–55. doi:10.1016/j.jfluidstructs.2011.10.006.
- Richardson, L.F., Gaunt, J.A., 1927. The deferred approach to the limit. Philosophical Transactions of the Royal Society A doi:<https://doi.org/10.1098/rsta.1927.0008>.
- Shirakashi, M., Mizuguchi, K., Bae, H.M., 1989. Flow-induced excitation of an elastically-supported cylinder caused by another located downstream in cruciform arrangement. Journal of Fluids and Structures 3, 595–607. doi:10.1016/S0889-9746(89)90150-3.
- Spalart, P., Allmaras, S., 1992. A one-equation turbulence model for aerodynamic flows, in: 30th Aerospace Sciences Meeting and Exhibit. URL: <http://arc.aiaa.org/doi/10.2514/6.1992-439>, doi:10.2514/6.1992-439, arXiv:arXiv:1011.1669v3.
- Stern, F., Wilson, R.V., Coleman, H.W., Paterson, E.G., 2001. Comprehensive approach to verification and validation of CFD simulations^{if}; part 1: methodology and procedures. Journal of fluids engineering 123, 793–802.
- Sun, H., Kim, E.S., Nowakowski, G., Mauer, E., Bernitsas, M.M., 2016. Effect of mass-ratio, damping, and stiffness on optimal hydrokinetic energy conversion of a single, rough cylinder in flow induced motions. Renewable Energy 99, 936–959. URL: <http://www.sciencedirect.com/science/article/pii/S0960148116306206>, doi:10.1016/j.renene.2016.07.024.
- Sun, H., Ma, C., Kim, E.S., Nowakowski, G., Mauer, E., Bernitsas, M.M., 2019. Flow-induced vibration of tandem circular cylinders with selective roughness: Effect of spacing, damping and stiffness. European Journal of Mechanics, B/Fluids 74, 219–241. doi:10.1016/j.euromechflu.2018.10.024.
- Wen, C., Wang, J., Zhang, Y., Xu, T., Zhang, X., Ning, Y., 2020. Vehicle Trajectory Clustering and Anomaly Detection at Freeway Off-Ramp Based on Driving Behavior Similarity, in: CICTP 2020, American Society of Civil Engineers, Reston, VA. pp. 4220–4232. URL: <http://ascelibrary.org/doi/10.1061/9780784482933.362>, doi:10.1061/9780784482933.362.
- Wu, W., 2011. Two-Dimensional RANS Simulation of Flow Induced Motion of Circular Cylinder with Passive Turbulence Control. Doctoral dissertation. The University of Michigan.
- Zhang, B., Mao, Z., Song, B., Ding, W., Tian, W., 2018. Numerical investigation on effect of damping-ratio and mass-ratio on energy harnessing of a square cylinder in FIM. Energy 144, 218–231. URL: <https://www.scopus.com/inward/record.uri?eid=2-s2.0-85037995662&doi=10.1016%2Fj.energy.2017.11.153&partnerID=40&md5=01db7c6b6d4d44e88de7045843c7d423>, doi:10.1016/j.energy.2017.11.153.
- Zhao, M., Lu, L., 2018. Numerical simulation of flow past two circular cylinders in cruciform arrangement. Journal of Fluid Mechanics 848, 1013–1039. URL: https://www.cambridge.org/core/product/identifier/S0022112018003804/type/journal_article, doi:10.

